Nano Energy 48 (2018) 266–274

Contents lists available at ScienceDirect

Nano Energy

journal homepage: www.elsevier.com/locate/nanoen

Communication

Flexible transparent aerogels as window retrofitting films and optical elements with tunable birefringence

Qingkun Liu[a], Allister W. Frazier[b], Xinpeng Zhao[c], Joshua A. De La Cruz[b], Andrew J. Hess[a], Ronggui Yang[c,d], Ivan I. Smalyukh[a,b,e,*]

[a] Department of Physics, Soft Materials Research Center and Department of Electrical, Computer, and Energy Engineering, University of Colorado, Boulder, CO 80309, USA
[b] Materials Science and Engineering Program, University of Colorado, Boulder, CO 80309, USA
[c] Department of Mechanical Engineering, University of Colorado, Boulder, CO 80309, USA
[d] Buildings and Thermal Systems Center, National Renewable Energy Laboratory, Golden, CO 80401, USA
[e] Renewable and Sustainable Energy Institute, National Renewable Energy Laboratory and University of Colorado, Boulder, CO 80309, USA

ARTICLE INFO

Keywords:
Aerogel
Cellulose nanofiber
Liquid crystal
Thermal insulation
Transparent

ABSTRACT

Experimental realization of optically transparent, mechanically robust and flexible aerogels has been a long-standing challenge, which limits their practical applications in energy-saving devices, such as thermally insulating films for enhancing energy efficiency of windows. The poor transparency precluded even hypothetical consideration of the possibility of birefringent aerogels. We develop birefringent and optically isotropic aerogels that combine properties of thermal super-insulation, mechanical robustness and flexibility, and transparency to visible-spectrum light. This unusual combination of physical properties is achieved by combining liquid crystalline self-organization of cellulose nanofibers with polysiloxane cross-linking and control of the nanoscale porosity to form hybrid organic-inorganic mesostructured aerogels. Potential applications of these inexpensive materials range from single pane window retrofitting to smart fabrics.

1. Introduction

Optical transparency, mechanical flexibility and robustness are among the physical properties that were long considered to be incompatible with aerogels, limiting practical applications of this class of porous mesostructured materials [1–3]. For example, the superior thermal insulation properties of aerogels, with a low thermal conductivity often lower than that of air, could be of interest for retrofitting inefficient single-pane windows of buildings or as viewing windows of various high temperature chambers and cryogenic setups. However, because of exhibiting porous mesomorphic structures and comprising mostly air, with a low volume fraction of solid nanoparticles assembled into a random loosely connected three-dimensional (3D) network, aerogels are commonly brittle and hazy [1–3]. To overcome these limitations, numerous strategies to mechanically strengthen the gelatinous skeletons have been explored, including crosslinking the polymeric network with organosilica precursors and implementation of synthetic or biopolymer-based aerogels [4–11]. Recent advances show that organosilica aerogels can exhibit excellent transparency with improved tolerance to compression and bending deformations, especially when using tri-functional or ethylene-bridged organosilica precursors, along with surfactants in aqueous solution under controlled gelation conditions [5,6]. To improve the mechanical robustness and flexibility of aerogels, various flexible polymeric networks have been utilized in recent studies, including melamine-formaldehyde, resorcinol-formaldehyde, various cellulose derivatives and cellulose nanofibers [7–9]. However, prior to gelation, a coarsened random porous structure often arises. In conjunction with the various bundles and clusters of nanofibers crosslinked directly by hydrogen bonds, this porous structure tends to strongly scatter light, yielding opaque or translucent aerogels. Organic-inorganic hybrid systems of transparent organosilica networks and flexible cellulose nanofibers have been identified as promising platforms to overcome these effects. These hybrid systems enable the fabrication of mechanically robust and flexible aerogels [10,11]. Nevertheless, meticulous control over the geometry and surface properties of fibers, the morphology of the gel's skeletal networks and the gelation conditions of this composite is essential to ensure the highest degree of structural homogeneity needed to suppress Mie scattering and substantially reduce Rayleigh scattering from the network and, thus, is crucial to obtain transparent aerogels. Furthermore,

* Corresponding author at: Department of Physics, Soft Materials Research Center and Department of Electrical, Computer, and Energy Engineering, University of Colorado, Boulder, CO 80309, USA.
E-mail address: ivan.smalyukh@colorado.edu (I.I. Smalyukh).

https://doi.org/10.1016/j.nanoen.2018.03.029
Received 12 December 2017; Received in revised form 12 February 2018; Accepted 9 March 2018
Available online 11 March 2018

fabrication of highly transparent mesoporous structures with varying degrees of orientational ordering of nanofibers would open up the possibility to engineer birefringent aerogels, though the traditionally poor transparency of aerogel materials precluded even hypothetical consideration of this possibility in the prior literature.

In this work, we develop highly transparent and flexible cellulose nanofiber-polysiloxane composite aerogels featuring enhanced mechanical robustness, tunable optical anisotropy, and low thermal conductivity. These characteristics are achieved by employing strictly controlled dimensions of nanofibers and the homogeneous gel skeleton networks that they form, which can be tuned to form orientationally ordered liquid crystal (LC) states. In the gel fabrication process, we employed and optimized an acid/base catalyzed sol-gel reaction in a surfactant-based solution to form the polymethylsilsesquioxane (PMSQ, $(CH_3SiO_{1.5})_n$) network. The cellulose nanofibers of uniform diameter were surface functionalized first with small charged molecules or by polymer grafting, both of which increased the cellulose nanofiber stability in tri-functional silane precursor solutions. Subsequently, these were crosslinked with PMSQ fibers. In addition to their high optical transparency, super thermal insulation, flexibility and mechanical robustness, our hybrid aerogels can be made optically isotropic or anisotropic, depending on the application. In the latter case, they are fabricated starting from the LC states of colloidal dispersions of nanofibers and may lead to practical applications in a new breed of optical polarization devices where the control of visible light's polarization must include simultaneous thermal insulation. Along with many other emerging cellulose-based advanced optical, plasmonic and photonic materials [12–22], our findings expand the scope of economical nanocellulose platforms for obtaining highly desirable photonic materials using self-assembly. Potential applications include various smart windows and reflective filters for the climate control and architectural appeal in buildings and smart fabrics for novel fashion and comfort designs, which were previously thought inaccessible because of the lack of materials with the unusual combination of properties that we have achieved, as well as because of the cost and scalability concerns that we mitigate through the means of using self-assembly.

2. Experimental methods

2.1. Synthesis of TOCNs

The cellulose nanofibers were produced through the oxidation of native cellulose by selectively modifying the C6 primary hydroxyl groups on the surface of native cellulose to carboxylate groups catalyzed by 2,2,6,6-tetramethylpiperidine-1-oxyl radical (TEMPO) under mild pH aqueous conditions, known as TEMPO-oxidized cellulose nanofibers (TOCNs) [23]. TOCNs each with the dimensions of 4.8 nm by several micrometers were synthesized using bleached wood cellulose by following the modified procedures described elsewhere in the literature [9]. Briefly, wood-cellulose-based bleached coffee filter (1 g) was suspended in 0.05 M sodium phosphate buffer (90 mL, pH 6.8) by dissolving 16 mg of TEMPO and 1.13 g of 80% sodium chlorite in a flask. Then 455 μL of NaClO solution (13% active chlorine) was diluted ten times with the same 0.05 M buffer used as the oxidation medium and was added at one step to the flask. The flask was immediately stoppered, and the suspension was stirred at 500 rpm at 60 °C for 120 h. After cooling the suspension to room temperature, the TEMPO-oxidized cellulose fibrils were thoroughly washed with water by centrifugation at 8700 rpm for 30 min. TEMPO-pretreated cellulose fibrils were then diluted at 0.25 wt%, mechanically blended at 28,000 rpm by a food processor (Versa Pro, from Oster), homogenized by a tip sonifier (S-450, from Branson) and filtered by a membrane filter with a pore-size of 11 μm. The resulting transparent solution was then concentrated by a rotary evaporator (R-200, from Buchi) at 60 °C.

2.2. Surface modification of TOCNs

The surface of TOCNs could be functionalized by simple physical adsorption of allylamine. Typically 500 mg of 0.2 wt% TOCNs aqueous solution was diluted by 2 mL of deionized (DI) water and mixed with 10 mg of allylamine. The mixture was stirred overnight and dialyzed for 2 days in a DI water bath across a cellulose acetate membrane with a cutoff molecular weight of 12,000–14,000 g/mol to obtain allylamine-TOCNs. To covalently bond the surface of TOCNs with cationic groups such as quaternary amine (QA), the carboxylate groups on TOCNs are linked with carbamoylcholine chloride via amidation. Briefly, 500 mg of 0.38 wt% aqueous TOCN dispersion was diluted by 2 mL of DI water and followed by the addition of 24 mg of 1-[Bis(dimethylamino) methylene] − 1H-1,2,3-triazolo[4,5-b]pyridinium 3-oxid hexafluorophosphate (HATU), 20 μL of N,N-Diisopropylethylamine (DIPEA), 50 mg carbamoylcholine chloride and 40 μL Dimethylformamide (DMF). The mixture was stirred for 2 days and dialyzed for another 2 days, which produced well-dispersed QA-TOCNs. Highly water soluble methoxy polyethylene glycol amine (mPEG-amine) could also be grafted onto the TOCN surface with the same amidation mechanism utilized to decorate the TOCN surface with QA moieties. Typically, 500 mg of 0.2 wt% TOCNs aqueous solution was diluted by 2 mL of DI water and followed by mixing with 28 mg of HATU, 20 μL of DIPEA, 18 mg mPEG-amine (MW = 5000) and 40 μL DMF. The mixture was stirred for 2 days and then dialyzed for another 2 days to finally obtain mPEG-TOCNs. All of the functionalized TOCN dispersions were concentrated by a rotary evaporator to the desired concentration.

2.3. Preparation of TOCN-PMSQ aerogels

TOCN hydrogels were fabricated by cross-linking functional TOCNs with polysiloxane following modified procedures described elsewhere in literature [2]. Typically, 0.4 g cetyltrimethylammonium bromide (CTAB) and 3.0 g of urea were dissolved in 8 mL of DI water with sonication until the sol became homogeneous and followed by the addition of 2 mL of functionalized TOCNs at different concentrations, 1–5 mL of methyltrimethoxysilane (MTMS) and 0.01 mmol acetic acid under vigorous stirring. After stirring the MTMS hydrolysis reaction fluid for 30 min at room temperature, the sol was degassed in a vacuum oven and then transferred into a polystyrene petri dish with a diameter of 5 cm, sealed for gelation and allowed to age for 3 days in a 60 °C furnace. The hydrogel was taken from the mold, immersed in DI water for 24 h to remove the urea and CTAB and subsequently followed by solvent exchange with isopropanol, which was replaced every 12 h at 60 °C for 2 days. Isopropanol was used as an intermediate solvent to replace water with liquid CO_2 without altering the mesostructured morphology of the wet gels. Isopropanol was chosen because it is miscible with both water and liquid CO_2, allowing one to avoid phase separation and modifications of mesostructured gel morphology due to interfacial tension. Finally, CO_2 supercritical drying at 38 °C under 8.6 MPa was conducted to obtain dried aerogel samples in a critical point dryer (Samdri-780A, from Tousimis). Aerogels of bulk densities ranging from 30 to 200 mg/cm^3 were prepared by varying the amount of MTMS. Moreover, a density of 69 mg/cm^3 was found to promote optimal optical transmittance and mechanical flexibility. Special care was taken to ensure that no stress was introduced to TOCN-PMSQ aerogel during processing.

2.4. Optical and electron imaging and spectra characterization

For both polarized and unpolarized brightfield optical microscopic imaging, an Olympus BX-51 polarizing optical microscope was equipped with 10 ×, 20 ×, and 50 × air objectives with a numerical aperture NA = 0.3–0.9 and a CCD camera Spot 14.2 ColorMosaic (Diagnostic Instruments, Inc.). Transmittance spectra were obtained using a spectrometer USB2000-FLG (Ocean Optics) mounted on the

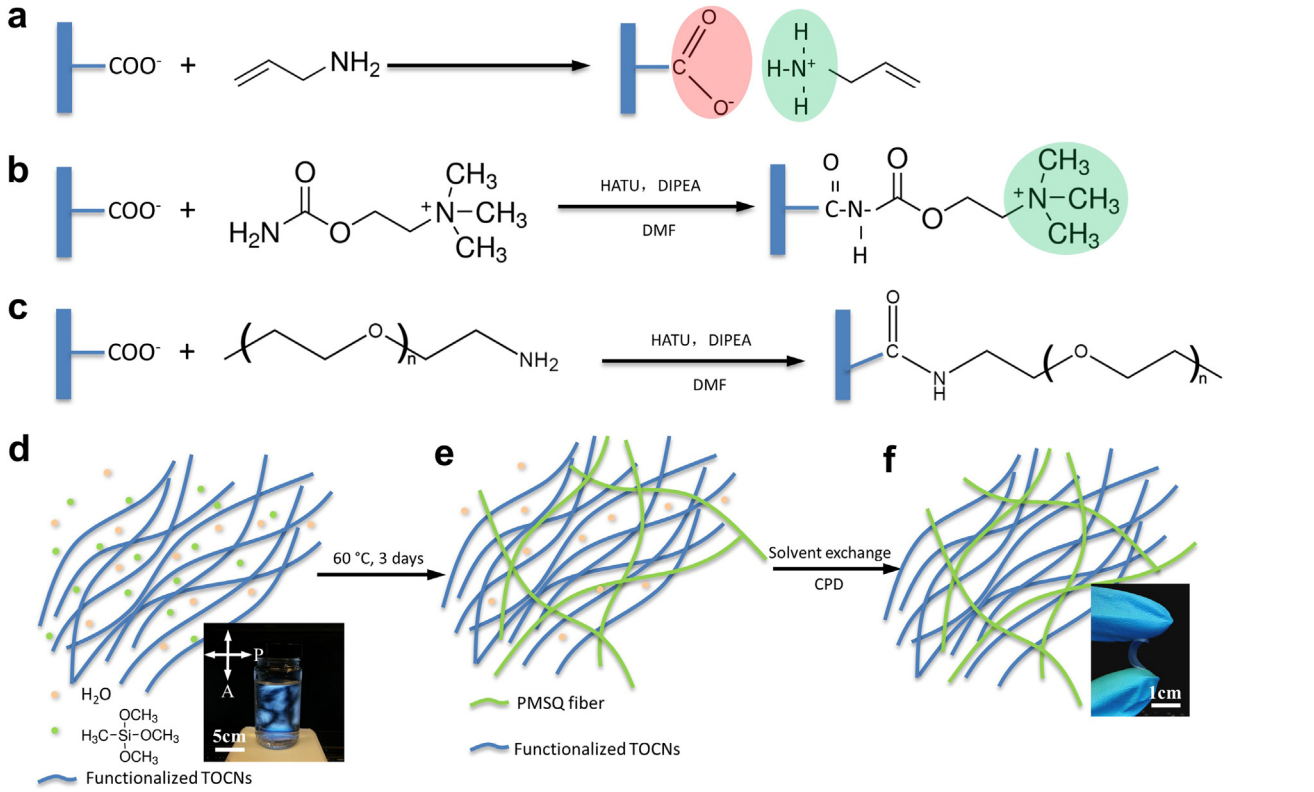

Fig. 1. Preparation of flexible transparent hybrid aerogels. (a-c) Schematic illustrating surface functionalization of TOCNs with (a) allylamine, (b) quaternary amine, and (c) mPEG-amine. (d–f) A schematic showing the gelation and transformation of anisotropic, liquid crystalline TOCNs crosslinked by PMSQ fibers from (d) precursor solution to (e) hydrogel and finally to (f) aerogel. Inset of (d): colloidal TOCNs present at relatively high concentrations in aqueous media observed between two crossed polarizers; inset of (f): a photograph of the flexible TOCN-PMSQ aerogel.

microscope. For light transmittance and haze measurements of aerogels, a UV–VIS–NIR spectrometer, ranging from 190 nm to 3200 nm, (UV-3101 pc, from Shimadzu) equipped with a LabSphere brand integrating sphere attachment was employed. Haze is defined as the ratio of diffuse transmittance to total transmittance, where diffuse transmittance is defined as transmitted light varying by greater than or equal to a 5° separation from the direction of incident light. Infrared (IR) transmittance spectra from wavenumbers 400 cm^{-1} to 4000 cm^{-1} (wavelengths 2.5–25 μm) and vibrational spectra of chemical bonds were recorded on a Fourier-transform infrared spectroscopy (FTIR) spectrometer (Nicolet AVATAR 370 DTGS, from Thermo) equipped with an a integrating sphere (NIR IntegratIR, from Pike). Photographs of samples were taken using a digital camera. IR thermographs were obtained by an IR camera (T630sc, from FLIR). Transmission electron microscopy (TEM) images were obtained using a CM100 microscope (from FEI Philips) at 80 kV. The TOCN samples were negatively stained with phosphotungstic acid to increase imaging contrast: 2 μL of the sample was dropcasted on the formvar coated copper grid, allowed to settle for drying and then dipped into the stain solution (aqueous 2 wt% phosphotungstic acid). The porous morphology of TOCN-PMSQ was characterized using an scanning electron microscopy (SEM) using a Hitachi Su3500 and Carl Zeiss EVO MA 10 system. For this, freshly cut surfaces of the TOCN-PMSQ aerogels were sputtered with a thin layer of gold and observed under SEM at a low voltage of 5 kV (as optimized to avoid the distortion of the aerogel samples). Nitrogen adsorption-desorption measurement was performed using ChemiSorb 2720 (from Micromeritics).

2.5. Thermal, mechanical, and durability characterization

The thermal conductivity is acquired by measuring both the heat capacity and thermal diffusivity of the aerogel samples. The heat capacity of aerogel is measured by differential scanning calorimetry (DSC 204 F1 Phoenix, Netzsch). The thermal diffusivity of aerogel is characterized by a laser flash apparatus (LFA 457, Netzsch). Briefly, an optical source instantaneously heats one side of the material and the temperature increment on the other side of the material is recorded by infrared thermography for facile, noninvasive temperature sensing. To prevent direct heating of the detector by laser light, the top and the bottom of the aerogel were covered with highly conductive carbon tape to prevent the laser from penetrating through the sample. The thermal conductivity of the aerogel can be calculated by subtracting the contribution of carbon tape from the effective thermal conductivity of the sandwich structure, which was determined by performing measurements for samples of different thickness. The Instron 5965 material test system was used to probe the mechanical properties and determine stress-strain relationships. The mechanical properties were measured with TOCN-PMSQ aerogel samples with 0.25 wt% QA-capped TOCN cut into rectangular strips of 20 mm × 6 mm × 1 mm. Aerogel durability testing was performed under a 500 W mercury lamp (Sun System 5, from Sunlight Supply Inc.) and in a Tenney environmental test chambers held at 80 °C and 80% relative humidity for 24 h.

3. Results

3.1. Liquid crystalline phase behavior of colloidal cellulose nanofibers

The nanofibers with a diameter of 4.8 nm and micrometer-scale lengths are stabilized in a basic solution by the Coulombic repulsion of their anionic carboxylate moieties, which overpower their tendency to form hydrogen bonds. As a result, the aqueous TOCN dispersions are highly transparent. To eliminate the strong light scattering originating from bundling and clustering of TOCNs which are uncontrollably crosslinked by direct hydrogel bonds, as often observed in polymeric

fibrous aerogels [8], we instead cross-link TOCNs with polysiloxane. This technique precludes direct contact between TOCNs and thereby generates a uniform nanofibrious network that exhibits small scattering cross-sectional areas. Hydrolysis of the polysiloxane precursor is acid-catalyzed. However, even under mildly acidic conditions and dilute concentrations, TOCNs tend to form a gel-like phase due to the hydrogen bonding between carboxylic acid functional groups [2]. To stably disperse TOCNs in polysiloxane precursor solutions, we implement various TOCN surface functionalization schemes, as illustrated in Fig. 1a–c. After TEMPO-mediated oxidation of cellulose, there exists a large density of carboxylic groups (~0.8 mmol/g) on the surface of nanofibrillated cellulose that is available for surface modification [23]. Briefly, the surface of cellulose nanoparticles can be altered by physical adsorption of molecules or by covalent bonding of small cationic molecules or polymeric chains in order to stabilize TOCNs via electrostatic repulsion or steric hindrance. The first strategy was readily realized by physisorption of cationic polyelectrolytic monomers, such as allylamine, to the anionic carboxylate groups of the cellulose. The cross-sectional diameter of TOCNs is not significantly affected by this method because of the small size of the molecules (Fig. 1a). The second TOCN surface functionalization strategy was implemented by amidation of the anionic carboxylate groups of TOCNs by introducing QA which decorate the nanocellulose surface with positively charged QA moieties (Fig. 1b). The successful functionalization of QA on TOCN surface was confirmed by the absorption peaks of C=O and N-H stretch in amide bond using FTIR. Lastly, polymers such as mPEG-amine were grafted on the TOCN surface by similar amidation and served as the final surface functionalization scheme detailed herein (Fig. 1c). These three methods are capable of improving colloidal-TOCN stabilization in the polysiloxane precursor solutions, which is key to achieving the novel physical behavior of our system that is discussed in further detail below.

The transparent surface-modified TOCNs' aqueous colloidal dispersions can exhibit LC ordering, which depends on the volume fraction of the nanofibers in the colloidal dispersion, and thus may exhibit birefringence when they are observed between crossed polarizers (inset of Fig. 1d). For the spontaneous nematic ordering of nanofibers to occur, the nanocellulose concentration must be above the critical concentration based on the Onsager theory [24–26]. Above this critical effective volume fraction $\phi_{cIN} \approx 4/l_{eff}$, predicted by the Onsager theory for charged rods [24–26], this order emerges to maximize the overall entropy of TOCNs, where l_{eff} is an effective aspect ratio of nanofiber length to its effective diameter, which is larger than the physical diameter to account for the electrostatic repulsions. Despite lowering the number of states associated with rotational degrees of freedom of colloidal nanofibers, this nematic state of the colloidal dispersions corresponds to an orientationally ordered state with low excluded volume and thus to a larger number of positional states accessible to TOCNs, maximizing the overall entropy at relatively high volume fractions of these colloidal dispersions. We estimate l_{eff} based on the extended Onsager theory for the isotropic-nematic phase transition of charged rods [27]. The Debye screening length ξ_D is estimated according to $\xi_D = (2\rho e^2/\varepsilon_0\varepsilon_r k_B T)^{-1/2}$, where $e = 1.6 \times 10^{-19}$ C is the elementary charge, $\rho = 10^{-4}$-10^{-2} M is the tunable bulk concentration of the electrolyte, $\varepsilon_0 = 8.85 \times 10^{-12}$ F/m is the vacuum permittivity, and $\varepsilon_r = 81$ (for water) is the relative permittivity of the solvent at 1 kHz, $k_B = 1.38 \times 10^{-23}$ J/K and $T = 300$ K is the absolute temperature. We estimate that ξ_D can be tuned within the range of 3–31 nm, consistent with the values reported in the literature [28]. Taking the concentration of carboxylate groups on the TOCN surface as 0.8 mmol/g, the density of cellulose as 1.5 g/cm^3 and the bare diameter D_c of TOCN as 4.8 nm, we also estimate the line charge density $\nu = 16.7$ e/nm [27]. The ratio of the effective TOCN diameter of D_{eff} and its bare diameter D_c is then given by $D_{eff}/D_c = 1 + (D_c/\xi_D)^{-1}(\ln A_0 + \gamma_E + \ln 2 - 1/2)$, where $\gamma_E \approx 0.577$ is Euler's constant and A_0 is dimensionless parameter [27]. For $D_c/\xi_D << 1$, we estimate $A_0 \approx 2\pi\nu^2\xi_D\lambda_B = 3.94 \times 10^4$, where $\lambda_B = e^2/4\pi\varepsilon_0\varepsilon_r k_B T = 0.74$ nm is the Bjerrum length. As a result, the ratio D_{eff}/D_c is calculated to be in the range within 8.3–74. The l_{eff} can then be re-expressed as $l_{eff} = (L_c/D_c)(D_{eff}/D_c)(1 - 3h/4)$, where $h = \xi_D/D_{eff} = (7.8–8.7) \times 10^{-2}$is the so-called electrostatic twist parameter and $L_c = 1200$ nm is the average TOCN length measured experimentally. The estimated l_{eff} for pH values within 10–12 is in the range of $(2.0–17) \times 10^3$ and $\phi_{cIN} \approx 4/l_{eff} = 0.02–0.2\%$. Because of the high bare length-to-width aspect ratio of TOCNs (~250) and because of the surface charging, the nematic LC phase behavior can emerge when TOCN volume fraction is as low as < 0.2%. From the standpoint of the design of composite aerogels, this behavior provides a unique possibility of imparting LC ordering at vanishingly low TOCN volume fractions which are critical for obtaining the desired optical anisotropy and other properties discussed below.

3.2. Realization of mesostructured hydrogels and aerogels

The surface-modified TOCNs are dispersed in a single tri-functional precursor MTMS solution and hydrolyzed under acidic conditions, followed by polysiloxane condensation in the basic solution formed by urea decomposition at 60 °C [5]. In this way, both the isotropic and liquid-crystalline arrangement, which depend on the surface-modified TOCN concentration, can be obtained. These orientationally ordered self-assembled structures can then be locked in and well-separated by isotropic PMSQ networks which are formed using a simple one-step sol–gel synthetic route. This procedure preserves the small and uniform cross-sections of individual fibers and their network (Fig. 1d–f) and, consequently, assures low light scattering.

Gelation results in a highly-transparent monolithic hydrogel of functionalized TOCNs, crosslinked by an isotropic, bicontinuous polysiloxane nanofibrious network (Fig. 2a). The transformation of hydrogels into transparent aerogels is accomplished via solvent exchange with isopropanol (Fig. 2b) and followed by critical point drying (Fig. 2c), as detailed in the experimental methods section. We considered three TOCN surface modification schemes (Fig. 1a–c) to optimize the transparency. Macroscopic clusters of TOCNs are observed in aerogels prepared with allylamine-capped TOCNs, resulting in relatively hazy aerogels due to the rather strong scattering from non-uniform morphology present at the mesoscopic scale (Fig. 2c). Aerogels comprised of polymer-grafted TOCNs, such as mPEG-amine via polysiloxane cross-linking, are also relatively hazy, which is partially due to the increased cross-sectional area of the polymer-grafted cellulose fibers (Fig. 2d). In contrast, QA-capped TOCN-PMSQ aerogels are highly transparent, featuring uniform morphology and a hint of blue appearance caused by the weak Rayleigh scattering of short-wavelength visible light, as expected due to their thin non-aggregated nanofiber scaffolds (Fig. 2e). All the measurements below are provided for QA-capped TOCN-PMSQ aerogels due to their superior optical transparency and low haze, though the two other surface functionalization strategies may still be of interest for applications where the requirements for high transparency and low haze characteristics are less critical.

3.3. Tunable birefringence and hydrophobicity

In addition to mechanical flexibility and robustness, many practical aerogel applications may require a high degree of hydrophobicity, for example, to assure that these aerogels are stable under ambient conditions and in humid environments). The QA-capped TOCN-PMSQ aerogels exhibit hydrophobic surface characteristics and a typical contact angle of 148°, largely due to the presence of hydrophobic methyl groups on the polysiloxane fibers within the nanostructured aerogels (Fig. 2f). An obvious advantage of our fabrication method is that there would be no need for post-synthetic hydrophobization treatment to enable such applications. The nematic ordering of the TOCN nanofiber network is preserved in the transparent aerogels above the critical TOCN concentration and manifests itself by imparting birefringence to the aerogel. Examples of polarizing optical micrographs of a

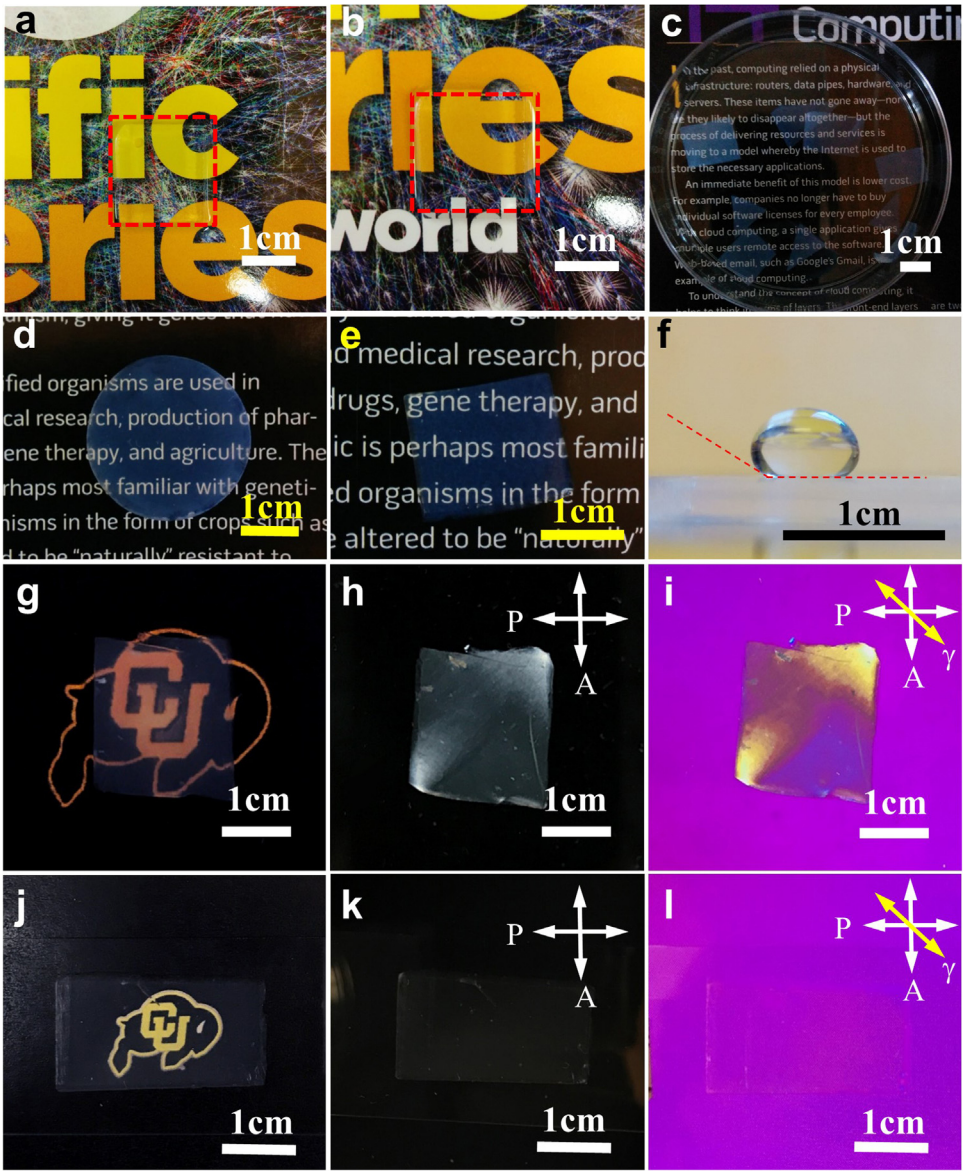

Fig. 2. Optically isotropic and birefringent, transparent and hydophobic aerogels. **a–c** Photographs showing transparent TOCN-PMSQ (a) hydrogel, (b) organogel (c) aerogel with allylamine-functionalized TOCNs. (d, e) TOCN-PMSQ aerogels with TOCN surfaces functionalized with (d) mPEG-amine and (e) QA species. (f) A photograph showing that the TOCN-PMSQ aerogel is hydrophobic, as evidenced by its high water-contact angle. (g) A photograph of a transparent birefringent TOCN-PMSQ aerogel with 0.28 wt% QA-capped TOCNs. and (j) isotropic TOCN-PMSQ aerogel with 0.01 wt % QA capped TOCNs. The corresponding polarized optical microscopy images obtained (h,k) before and (i,l) after the insertion of a 530 nm retardation plate, with a slow axis (γ) indicated by a yellow double-headed arrow.

transparent aerogel (Fig. 2g) obtained under crossed polarizers before and after the insertion of a 530 nm retardation waveplate are shown in Fig. 2h,i, respectively. At a concentration of aligned TOCNs of about 0.3 wt%, the optical anisotropy (defined as the difference between extraordinary and ordinary refractive indices) is given by $\Delta n \approx 1.6 \times 10^{-4}$, as measured using a 20λ Berek Compensator mounted on a polarizing optical microscope with objectives with different magnifications of 10 ×, 20 × and 50 ×, which averages the birefringence of the sample in the area from 40 μm^2 to 1 mm^2 [29]. By varying the volume fraction of TOCNs, the resulting optical anisotropy (birefringence) can be controlled within the accessible range of 5.3×10^{-6}-1.6×10^{-3}. For example, colloidal dispersions of 0.28 wt% TOCN in a 2.1-mm thick sample yield TOCN-PMSQ composite aerogels with a birefringence of 1.5×10^{-4}, giving the experimentally measured $\Delta n \cdot d \approx 320$ nm, where d is the thickness of the aerogel sample. This birefringence value indicates that such aerogels can be used as polarizing optical elements for visible and infrared light. Furthermore, unidirectional shearing of colloidal dispersions of TOCNs before their cross-linking provides a simple but robust means of controlling the LC director of the uniform orientation of the director of the lyotropic LC, which then defines the orientation of the optical axis of the effectively optically monocrystalline aerogels in the final product. The presence of small haze (~8%) also introduces depolarization and alters the overall polarization state of the transmitted light due to scattering effects. Optically isotropic and transparent TOCN-PMSQ aerogels can also be prepared (Fig. 2j–l) simply by lowering the TOCN concentration. For example, the highly transparent 3-mm thick TOCN-PMSQ aerogel (Fig. 2j), prepared with 0.01 wt% QA-capped TOCNs, is optically isotropic. This optical property is apparent when the latter aerogels are viewed between crossed polarizers (Fig. 2k,l).

3.4. Mesoscale morphologies and optical transparency

To investigate the structure-property relationship of TOCN-polysiloxane aerogels, the mesoscale morphology of the aerogels is characterized by electron microscopies. TEM observations reveal that the colloidal dispersions consist of mostly individualized TOCNs, each of diameter $D_c \approx 5$ nm and length L_c = 1–2 μm (Fig. 3a). SEM images reveals the well-defined and uniform-diameter 10–15 nm nanofibers that are formed by polysiloxane and individually dispersed TOCNs fibers within the aerogels as well as a narrow pore-size distribution of their resulting porous network (Fig. 3b,c). The aerogel samples exhibit 3D bicontinuous network-like structures, in which both the smooth gel skeletons and the pores are interconnected without aggregation or

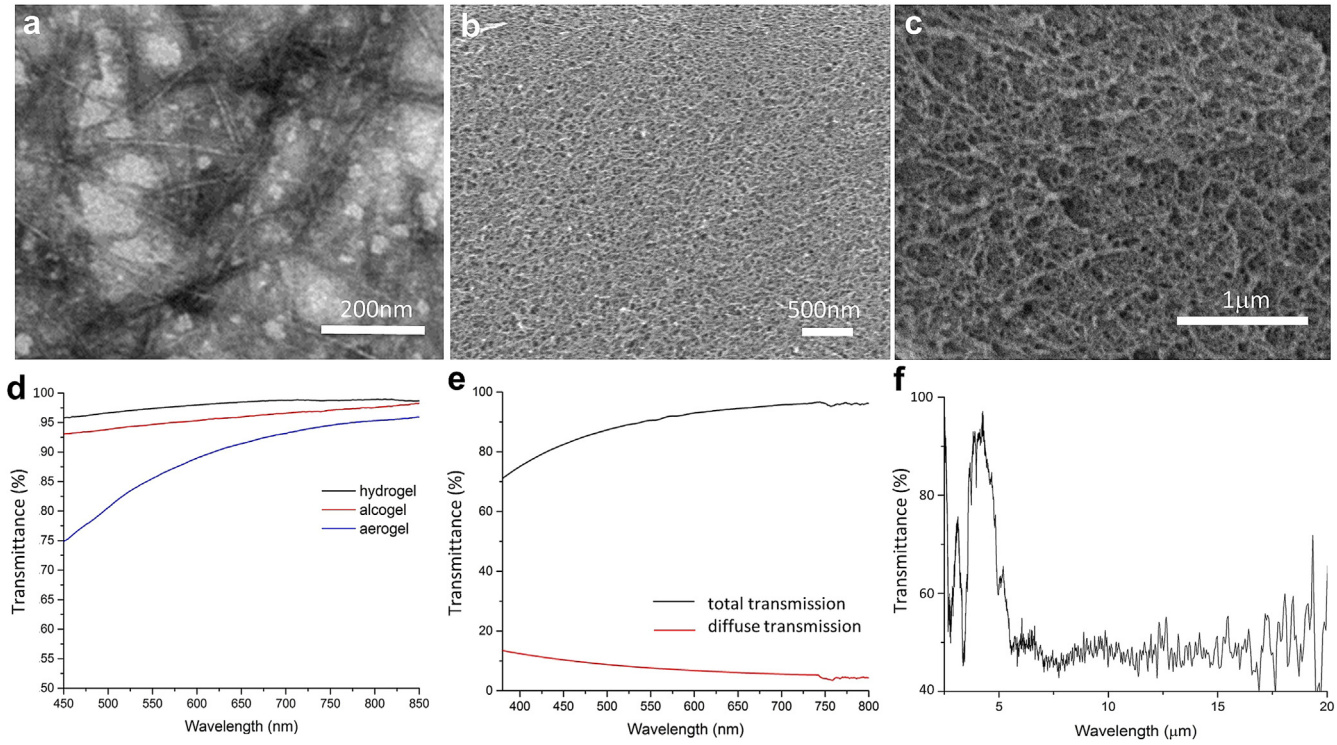

Fig. 3. Mesoscale morphologies and optical properties of TOCN-PMSQ aerogels. (a) Transmission electron micrographs of negatively stained TOCNs, and scanning electron micrographs of TOCN-PMSQ aerogels featuring TOCNs concentrations of (b) 0.03 wt% and (c) 0.06 wt%. (d) Transmittance of TOCN-PMSQ gels. (e) Total transmittance and diffuse transmittance light of TOCN-PMSQ aerogel. (f) IR transmittance of a TOCN-PMSQ aerogel with 0.06 wt% of TOCNs.

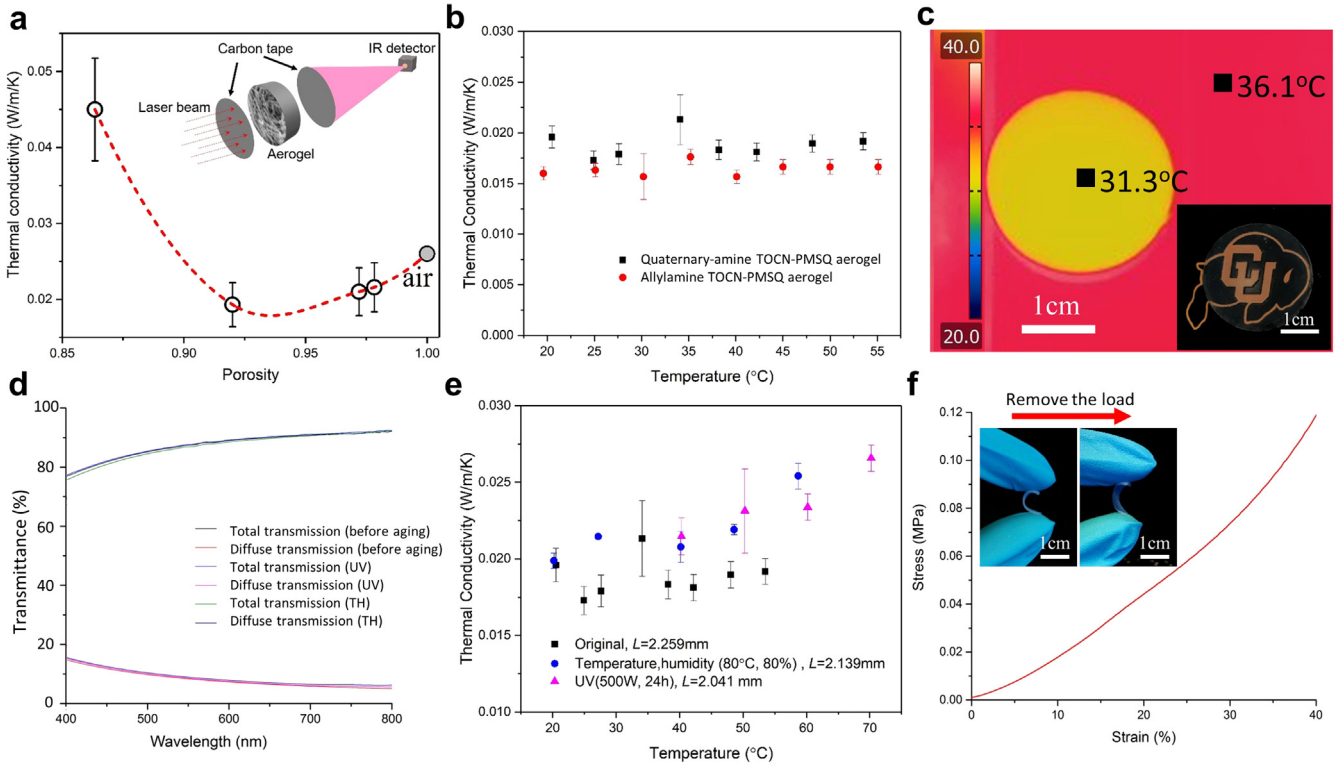

Fig. 4. Thermal, mechanical and durability properties of TOCN-PMSQ aerogels. (a) Measured thermal conductivity of TOCN-PMSQ aerogel versus sample porosity. The inset shows the principle of the thermal property measurement. (b) Thermal conductivities of TOCN-PMSQ aerogels before degradation testing. (c) Infrared thermograph of a TOCN-PMSQ aerogel on a hotplate. (d) Total and diffuse transmittance spectra (top and bottom-most sets of curves, respectively) before and after UV and elevated temperature/humidity degradation testing. (e) Thermal conductivity measured after aerogel subjected to degradation testing. (f) Compression stress-strain relation of the TOCN-PMSQ aerogel with 0.06 wt% of TOCNs. Inset: the same TOCN-PMSQ aerogel springs back upon removal of the load.

clustering. For the provided example (Fig. 3), the bulk density ρ_b is calculated to be 69 mg/cm^3 by weight/volume ratio of the sample. Porosity, defined as $\varepsilon = (1-\rho_b/\rho_s)\times 100\%$, is then determined to be $\varepsilon \approx 94.9\%$, where ρ_s is the skeletal density, taken to be 1.35 g/cm^3. The average pore size for this particular example is calculated to be approximately 100 nm, consistent with the value observed directly from the SEM images (Fig. 3a–c). SEM images of the aerogel samples taken at different areas across the square-inch samples all show uniform mesostructured morphology of the entire sample, consistent with transmission-mode optical images at larger scales. The specific surface area of aerogels was determined to be 685.9 m^2/g for the adsorption of nitrogen cycle and 606.8 m^2/g for the desorption of nitrogen cycle, consistent with the mesostructured morphology revealed by the SEM images. The mesoscale morphology of the 2.0-mm thick QA-capped TOCN-PMSQ composite aerogel with ultrathin fibers and uniform pore size distribution yields hydrogels and alcogels with very high light transmittance greater than 90% and aerogels with visible transmittance close to 90% at 600 nm (Fig. 3d). The aerogel's haze coefficient, defined as the ratio of diffuse transmittance and total light transmittance, is determined to equal to 8.4%, which is rather low for aerogels (Fig. 3e) and is characterized following the ASTM D1003 standard using an integrating sphere setup when integrated across the visible range (390–700 nm), shown in Supplementary Fig. 1 [30]. The PMSQ matrix causes TOCN-PMSQ aerogels to exhibit strong absorption at a wavelength of 6–20 μm, which is mainly due to a strong and broad Si–O vibrational mode at 1100 cm^{-1}, Si–C bonds at 840 cm^{-1} and 1310 cm^{-1}, and C–H bond at 1400 cm^{-1} (Fig. 3f) [31]. This provides an interesting possibility of separately controlling transmittance of visible and infrared light, which could be of interest for controlling solar gain and emissivity in smart-window applications.

3.5. Thermal, mechanical and durability properties of aerogels

The thermal conductivity of the aerogel samples was characterized by measuring thermal diffusivity using the laser flash method (see the experimental principle shown in the inset of Fig. 4a) and the heat capacity using the differential scanning method. The experimentally determined thermal conductivity versus sample porosity of the TOCN-PMSQ aerogels is shown in Fig. 4a. The thermal conductivity of our aerogels is lower than that of air for a rather broad range of solid volume fractions. Minimal values exist when the porosities are within 90–97 vol%. Interestingly, although the optical properties of QA-capped TOCN-PMSQ aerogels are better than those of allylamine-capped TOCN-PMSQ aerogels, the thermal properties of these two classes of aerogels are comparable. To study these properties in more details, QA- and allylamine-capped TOCN-PMSQ aerogels were prepared with a density of 69 mg/cm^3, chosen to minimize thermal conductivity and haze at the same time. For each sample, the thermal conductivity stays roughly constant as temperature is varied from 20 °C to 55 °C (Fig. 4b). Furthermore, we find that the thermal conductivity $\approx 0.018 \pm 0.003$ Wm^{-1}K^{-1} of QA-functionalized TOCN-PMSQ aerogels is close to that of allylamine-functionalized TOCN-PMSQ aerogels, which was measured to be $\approx 0.016 \pm 0.002$ Wm^{-1}K^{-1}, demonstrating that a thermal conductivity significantly less than that of air (0.026 Wm^{-1}K^{-1}, at 300 K and 1 atm) can be achieved in various ways. This super thermal insulation behavior is an inherent property typical for aerogels due to their nanoporous structure. The heat transport in aerogels includes contributions due to solid conduction, conduction of gas and radiation [32,33]. At room temperature, thermal radiation plays a negligible role. The heat transfer through a solid network of nanofibers increases as the porosity decreases (corresponding to increasing solid volume fractions). However, the proximity of a solid backbone of the aerogel fibers also reduces the thermal conduction of air molecules due to the rarefied gas effect. The gaseous phase thermal conductivity has an inverse relationship with the porosity, opposite to the relationship between solid-phase conduction and porosity. Consequently, the overall thermal conductivity is at minimum for porosities within 90–97% (Fig. 4a). The wide range of porosities that yield rather small thermal conductivity aids the optimization of the mesoporous morphology needed to obtain transparent aerogels that can also serve as effective thermal barriers. Infrared thermography of the transparent TOCN-PMSQ aerogel enables direct visualization of the effectiveness of TOCN-PMSQ aerogel as a thermal barrier (Fig. 4c). When the TOCN-PMSQ aerogel is placed directly on a hot stage, the surface temperature of the aerogel is considerably lower than that of the hot stage. For reference, the ambient room temperature was recorded to be 24.0 °C.

In addition to the tolerance of compression and bending deformations and hydrophobicity, practical applications like retrofitting single pane windows and clothing are limited by the ability of the material to withstand in its working environments over extended periods of time, on the scale of years. To predict how these materials will behave over their working lifetimes, we conduct accelerated degradation tests of our aerogels and investigate the interaction of the TOCN-PMSQ aerogel with ultraviolet (UV) radiation, elevated temperatures and high humidity. The 2 mm-thick QA-capped TOCN-PMSQ aerogel shows little to no change of optical and thermal properties after exposure to intense UV radiation from a 500-W mercury-vapor lamp, or after placement in an 80 °C/80% relative humidity chamber, in each case for 24 h (Fig. 4d,e). The visible-light transmittance and haze coefficients of the aerogels were averaged across 390–700 nm, as discussed above. After only UV aging, the changes of both transmittance and haze of the aerogel were determined to be within 1%, comparable to experimental error. After simultaneous aging of an identical sample in an 80 °C/80% relative humidity chamber but with no UV aging, the visible-light transmittance of the aerogel remained the same and the barely detectable change of haze was found to be within 1%. By comparing these metrics, measured before and after each aging process for a series of 10 samples, we conclude that there are no observable changes in optical performance beyond experimental error. To reinforce the notion that our TOCN-PMSQ aerogels are robust with respect to simulated environmental degradation, Fig. 4e compares the thermal conductivity of the aerogel before and after both durability tests and shows that the thermal conductivity does not appreciably change, indicating that our aerogels possess excellent thermal stability for their performance metrics. Moreover, by finding that the change in contact angle of the aerogel before and after aging is insignificant, we also conclude that the hydrophobic nature of TOCN-PMSQ aerogel is preserved as well.

A significant advantage of TOCN-PMSQ aerogels over their conventional silica counterparts is their mechanical robustness and resilience against compressive and bending mechanical deformations (inset of Figs. 1f and 4f). The compression stress–strain curves for the TOCN-PMSQ aerogels prepared with density 69 mg/cm^3 are shown in Fig. 4f, indicating elastic behavior at rather high strains of up to 40% with an applied stress of 120 kPa (Fig. 4f). Furthermore, the TOCN-PMSQ aerogels are flexible (inset of Fig. 1f), with the bending deformations being fully reversible because of their elastic characteristics, and remain pliable even after hundreds of repeated deformations (note that Fig. 4f insets show a deformed aerogel that relaxes upon removal of the load). These favorable mechanical properties enable the aerogels to be laminated atop of solid surfaces, which, for example, could be useful for the retrofitting of existing single-pane windows.

4. Conclusions

In conclusion, we have developed a new breed of hybrid aerogels combining chemically modified biopolymeric nanofibers with an inorganic polysiloxane network to form mesostructured nanoporous morphologies. The experimental platform we have developed allows us to prepare either optically isotropic or anisotropic, highly transparent hydrogels, organogels and aerogels whose birefringence is controlled by varying the concentration of cellulose nanofibers. The TOCN-PMSQ

aerogels are shown to be transparent, thermally insulating and mechanically flexible, a combination of properties not observed in conventional aerogels. Another key advantage of our aerogels is that their production is inexpensive and can be potentially scaled-up in future works, as the ordered nanostructure is produced with a bottom-up approach via self-assembly of colloidal dispersions. Since hydrogels, organogels and aerogels are all flexible, the critical point drying process, which we use to fabricate our aerogels, potentially can be done for large-area samples while they are rolled within the drying chamber. The techno-economic analysis of TOCN-PMSQ aerogel preparation, which we briefly describe in the supplementary material, shows that 2.7-mm-thick aerogels could be possibly fabricated at a cost of less than $5 per square foot. Therefore, we believe that this new breed of inexpensive aerogels may find a broad range of applications within optical-grade materials that feature tunable birefringence alongside robust thermal insulation. The described composite aerogel production process, which is economical and promises to be easily scalable because of its reliance on TOCN self-assembly, may allow for applications that were previously thought inaccessible to mesostructured porous materials, such as laminatable energy-saving films for window retrofitting, specialized polarizing optics and smart textiles.

Acknowledgements

We thank Dawei Zhang, Bohdan Senyuk and Blaise Fleury for discussions and Yao Zhai, Maxwell P. Brunette, David Rudman, Yinan Lu and Rong Long for technical assistance. This research was supported by the U.S. Department of Energy, ARPA-E award DE-AR0000743.

Competing interests

The authors declare no competing financial interests.

Appendix A. Supporting information

Supplementary data associated with this article can be found in the online version at http://dx.doi.org/10.1016/j.nanoen.2018.03.029.

References

[1] A.C. Pierre, G.M. Pajonk, Chemistry of aerogels and their applications, Chem. Rev. 102 (2002) 4243–4266.
[2] M. Aegerter, N. Leventis, M.M. Koebel, Aerogels Handbook, Springer Science & Business Media, 2011.
[3] R. Baetens, B.P. Jelle, A. Gustavsen, Aerogel insulation for building applications: a state-of-the-art review, Energy Build. 43 (2011) 761–769.
[4] K. Kanamori, K. Nakanishi, Controlled pore formation in organotrialkoxysilane-derived hybrids: from aerogels to hierarchically porous monoliths, Chem. Soc. Rev. 40 (2011) 754–770.
[5] K. Kanamori, M. Aizawa, K. Nakanishi, T. Hanada, New transparent methylsilsesquioxane aerogels and xerogels with improved mechanical properties, Adv. Mater. 19 (2007) 1589–1593.
[6] T. Shimizu, K. Kanamori, A. Maeno, H. Kaji, K. Nakanishi, Transparent ethylene-bridged polymethylsiloxane aerogels and xerogels with improved bending flexibility, Langmuir 32 (2016) 13427–13434.
[7] G. Hasegawa, T. Shimizu, K. Kanamori, A. Maeno, H. Kaji, K. Nakanishi, Highly flexible hybrid polymer aerogels and xerogels based on resorcinol-formaldehyde with enhanced elastic stiffness and recoverability: insights into the origin of their mechanical properties, Chem. Mater. 29 (2017) 2122–2134.
[8] Y. Kobayashi, T. Saito, A. Isogai, Aerogels with 3D ordered nanofiber skeletons of liquid-crystalline nanocellulose derivatives as tough and transparent insulators, Angew. Chem. Int. Ed. 126 (2014) 10562–10565.
[9] F. Fischer, A. Rigacci, R. Pirard, S. Berthon-Fabry, P. Achard, Cellulose-based aerogels, Polymer 47 (2006) 7636–7645.
[10] J. Cai, S. Liu, J. Feng, S. Kimura, M. Wada, S. Kuga, L. Zhang, Cellulose–silica nanocomposite aerogels by in situ formation of silica in cellulose gel, Angew. Chem. Int. Ed. 124 (2012) 2118–2121.
[11] G. Hayase, K. Kanamori, K. Abe, H. Yano, A. Maeno, H. Kaji, K. Nakanishi, Polymethylsilsesquioxane–cellulose nanofiber biocomposite aerogels with high thermal insulation, bendability, and superhydrophobicity, ACS Appl. Mater. Interfaces 6 (2014) 9466–9471.
[12] K.E. Shopsowitz, H. Qi, W.Y. Hamad, M.J. MacLachlan, Free-standing mesoporous silica films with tunable chiral nematic structures, Nature 468 (2010) 422–425.
[13] Q. Liu, M.G. Campbell, J.S. Evans, I.I. Smalyukh, Orientationally ordered colloidal co-dispersions of gold nanorods and cellulose nanocrystals, Adv. Mater. 26 (2014) 7178–7184.
[14] M. Nogi, S. Iwamoto, A.N. Nakagaito, H. Yano, Optically transparent nanofiber paper, Adv. Mater. 21 (2009) 1595–1598.
[15] Z. Nie, A. Petukhova, E. Kumacheva, Properties and emerging applications of self-assembled structures made from inorganic nanoparticles, Nat. Nanotechnol. 5 (2010) 15–25.
[16] S.N. Fernandes, P.L. Almeida, N. Monge, L.E. Aguirre, D. Reis, C.L. de Oliveira, A.M. Neto, P. Pieranski, M.H. Godinho, Mind the microgap in iridescent cellulose nanocrystal films, Adv. Mater. 29 (2017).
[17] E. Cudjoe, M. Younesi, E. Cudjoe, O. Akkus, S.J. Rowan, Synthesis and fabrication of nanocomposite fibers of collagen-cellulose nanocrystals by coelectrocompaction, Biomacromolecules 18 (2017) 1259–1267.
[18] D.X. Oh, Y.J. Cha, H.L. Nguyen, H.H. Je, Y.S. Jho, D.S. Hwang, D.K. Yoon, Chiral nematic self-assembly of minimally surface damaged chitin nanofibrils and its load bearing functions, Sci. Rep. 6 (2016) 23245.
[19] Q. Liu, I.I. Smalyukh, Liquid crystalline cellulose-based nematogels, Sci. Adv. 3 (2017) e1700981.
[20] T.D. Nguyen, W.Y. Hamad, M.J. MacLachlan, Near-IR-sensitive upconverting nanostructured photonic cellulose Films, Adv. Opt. Mater. 5 (2017).
[21] H. Yano, J. Sugiyama, A.N. Nakagaito, M. Nogi, T. Matsuura, M. Hikita, K. Handa, Optically transparent composites reinforced with networks of bacterial nanofibers, Adv. Mater. 17 (2005) 153–155.
[22] M.G. Campbell, Q. Liu, A. Sanders, J.S. Evans, I.I. Smalyukh, Preparation of nanocomposite plasmonic films made from cellulose nanocrystals or mesoporous silica decorated with unidirectionally aligned gold nanorods, Materials 7 (2014) 3021–3033.
[23] T. Saito, M. Hirota, N. Tamura, S. Kimura, H. Fukuzumi, L. Heux, A. Isogai, Individualization of nano-sized plant cellulose fibrils by direct surface carboxylation using TEMPO catalyst under neutral conditions, Biomacromolecules 10 (2009) 1992–1996.
[24] L. Onsager, The effects of shape on the interaction of colloidal particles, Ann. N. Y. Acad. Sci. 51 (1949) 627–659.
[25] P.M. Chaikin, T.C. Lubensky, Principles of Condensed Matter Physics, Cambridge Univ. Press, 2000.
[26] H.N.W. Lekkerkerker, G.J. Vroege, Liquid crystal phase transitions in suspensions of mineral colloids: new life from old roots, Philos. Trans. R. Soc. A 371 (2013) 20120263.
[27] G.J. Vroege, H.N.W. Lekkerkerker, Phase transitions in lyotropic colloidal and polymer liquid crystals, Rep. Prog. Phys. 55 (1992) 1241.
[28] H. Fukuzumi, R. Tanaka, T. Saito, A. Isogai, Dispersion stability and aggregation behavior of TEMPO-oxidized cellulose nanofibrils in water as a function of salt addition, Cellulose 21 (2014) 1553–1559.
[29] T. Scharf, Polarized Light in Liquid Crystals and Polymers, John Wiley & Sons, 2007.
[30] B. Geometries, S. Abrasion, Standard test method for haze and luminous transmittance of transparent plastics, ASTM Int. 1 (2012) 1–7.
[31] M.A. Aegerter, N. Leventis, M.M. Koebel, Aerogels Handbook, Springer Science & Business Media, 2011.
[32] X. Lu, M.C. Arduini-Schuster, Thermal conductivity of monolithic organic aerogels, Science 255 (1992) 971.
[33] Z.Y. Li, H. Liu, X.P. Zhao, W.Q. Tao, A multi-level fractal model for the effective thermal conductivity of silica aerogel, J. Non-Cryst. Solids 430 (2015) 43–51.

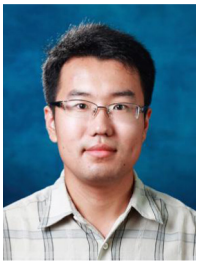

Qingkun Liu obtained his BS degree in Optics from the University of Electronic Science and Technology of China (2007) and Ph.D. degree in Optical Engineering from Zhejiang University (2013). He joined in Department of Physics of the University of Colorado-Boulder as a research associate in 2013, where he also was a visiting scholar since 2008. His current research focuses on nanostructured and biological soft matter, including nanocellulose, liquid crystals, colloids, nanomaterials, etc.

Allister W. Frazier obtained his BS degree in Physics from the University of Nevada, Reno (2016). He is currently a Ph.D. student in Materials Science and Engineering at the University of Colorado Boulder. His research focuses on the design and fabrication of cellulose-based aerogels and production of nanocellulose from bacterial cellulose using sustainable resources.

Xinpeng Zhao received his BS degree at Northwestern Polytechnical University in 2012 and MS degree at Xi'an Jiaotong University in 2015. He is currently a Ph.D. student in Mechanical Engineering at University of Colorado Boulder. His research focuses on modeling, simulation and experimental characterization of thermal transport in thermal insulation materials such as aerogels and nanowoods.

Joshua A. De La Cruz obtained his BS degree in Materials Science and Engineering from the University of Arizona (2014) and MS degree in Materials Science and Engineering from the University of Colorado Boulder (2016). He is currently a Materials Science and Engineering Ph.D. student at the University of Colorado and his research focuses on cellulose-based biomimetic photonic structures used for energy-saving technologies.

Andrew J. Hess obtained his BS degree in Physics from the Department of Physics and Astronomy at Calvin College (2013), a MS degree in Physics, and a Renewable Energy Certificate from the University of Colorado Boulder (2016). He is currently a Physics Ph.D. candidate at the University of Colorado Boulder and his research focuses on the study of liquid crystals, including liquid crystalline polymers, colloids, solitons and gels.

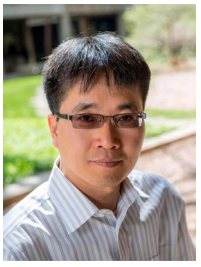

Ronggui Yang obtained a BS in Thermal Engineering from Xi'an Jiaotong University (1996), a MS in Thermal Engineering from Tsinghua University (1999), a MS in Micro-Electro-Mechanical Systems from The University of California, Los Angeles (2001) and a Ph.D. in Mechanical Engineering from MIT (2006). He started his faculty career as an Assistant Professor at the University of Colorado Boulder (CU-Boulder) in January 2006, was promoted to Associate Professor in 2011 and to Full Professor in 2016. He currently directs the Nano-enabled Energy Conversion and Thermal Management Systems group (NEXT) at CU-Boulder. His research interests are on the fundamentals of nanoscale transport phenomena (thermal, electrical, thermoelectric, phase-change) and applications of micro/nanotechnologies to thermal, energy and water systems. Dr. Ronggui Yang has published ~ 140 journal papers, with an h-Index of 44, a total citation > 9000 times per Google Scholar. He is an elected ASME Fellow.

Ivan I. Smalyukh obtained BS and MS degrees from Lviv Polytechnic National University (1995) and Ph.D. from Kent State University (2003). He was a postdoctoral research associate at the University of Illinois Urbana-Champaign. He joined the Department of Physics at CU-Boulder as an Assistant Professor in 2007, was promoted to Associate Professor in 2014 and Full Professor in 2017. He is a fellow of Renewable Sustainable Energy Institute and Materials Science Engineering Program and directs the Soft Matter Physics Group at CU-Boulder. His research focuses on soft matter and biological systems, including liquid crystals, colloids, polymers, bacteria, gels, biomaterials and their photonic, electro-optic and energy-related applications. He published ~160 papers and has an h-index of 44. He is a fellow of the American Physical Society (APS). He received many awards, including the Bessel and Glenn Brown Awards, the PECASE Award from the White House and the GSoft Award from APS.